Progress in Organic Coatings 175 (2023) 107370

Contents lists available at ScienceDirect

Progress in Organic Coatings

journal homepage: www.elsevier.com/locate/porgcoat

Enhanced wear resistance while maintaining transparency of epoxy resin coatings filled with novel one-dimensional magnesium borate hydroxide nanorods

Na Li [a,b,1], Na Li [c,d,1], Zhi-qi Liu [a,e,*], Yun-xian Yang [f], Yong-cang Ying [e], Zi-yuan Zhou [e]

[a] Green Industry Innovation Research Institute, Anhui University, Hefei, Anhui 230000, China
[b] Qinghai Institute of Salt Lakes, Chinese Academy of Sciences, Xining 810008, China
[c] LNM, Institute of Mechanics, Chinese Academy of Sciences, Beijing 100190, China
[d] IMDEA Materials Institute, C/Eric Kandel, 2, 28906 Getafe, Madrid, Spain
[e] School of Chemistry & Chemical Engineering, Anhui University, Anhui 230601, China
[f] Advanced Research Institute of Multidisciplinary Sciences and State Key Laboratory of Explosion Science and Technology, Beijing Institute of Technology, Beijing 100081, PR China

ARTICLE INFO

Keywords:
Epoxy resin
Transparency
Scratch resistance
Nanoscratch
Nanocoating

ABSTRACT

Wear resistance and transparency are critical properties of polymer coatings. In this study, a novel nanocoating filler composed of one-dimensional inorganic magnesium borate hydroxide (MBH) nanorods was used to improve the wear resistance and transparency of epoxy resin (EP) coatings. After successfully synthesizing MBH nanorods, different amounts were added to EP coatings to prepare EP/MBH nanocomposites, denoted as ExMBH (x = 1, 5, and 10 wt% MBH). The transparency and wear resistance of the neat and MBH-filled EP coatings were estimated using optical transmittance and nanoscratch testing, respectively. The results indicate that E10MBH displays a transmittance of more than 85 % in the visible region and a low value in the UV region, resulting from the similar refractive indices of the MBH filler and EP. Additionally, the scratch recovery index and scratch hardness increase by 53 % and 22 %, respectively, while the plastic deformation energy decreases by 67 % compared to that of the neat EP coating. The E10MBH nanocoating presents excellent wear resistance due to the formation of a solid three-dimensional network structure between EP and MBH. This paper demonstrates an effective strategy for designing inorganic nanofillers to improve the mechanical durability and optical properties of EP nanocoatings.

1. Introduction

Because of their eco-friendliness, chemical resistance, high adhesion, and low costs, epoxy resin (EP) coatings are frequently employed in optical devices, electric appliances, and architecture [1,2]. Nevertheless, they are vulnerable to scratching and perforation because of their low Young's modulus and wear resistance, which limits their wider application as coatings [1]. Thus, extensive research has been focused on improving the wear resistance of EP coatings by incorporating inorganic and organic polymer nanoparticles into the EP matrix, which can produce nanocoatings with enhanced mechanical performance.

Considering organic polymer nanocomposites, the mechanical robustness and long-term durability of EP coatings have been improved using waste tire rubber, carbon nanotubes, carbon nanofibers, graphene, and fluoroepoxy oligomers as filler materials. In particular, crosslinks form between wrinkled graphene flakes and the polymer matrix, thereby increasing the mechanical and tribological strength of the EP. However, the dispersion of the incorporated reinforcing agents is usually poor, particularly at higher volumes, which leads to aggregation, decreased transparency, and environmental pollution. Moreover, using lower volumes of organic nanofillers to circumvent the clustering of reinforcements only provides a limited enhancement effect.

To improve wear resistance further, numerous studies have investigated filling polymeric materials with inorganic nanoparticles, such as TiO_2 and SiO_2 nanofillers [3–6]. In addition to the inherent hardness of the inorganic filler, the composite strengthening mechanisms are

* Corresponding author at: School of Chemistry & Chemical Engineering, Anhui University, Hefei, Anhui 230039, China.
E-mail address: 20018@ahu.edu.cn (Z.-q. Liu).
[1] These authors contributed equally to this work and should be considered co-first authors.

https://doi.org/10.1016/j.porgcoat.2022.107370
Received 7 October 2022; Received in revised form 28 November 2022; Accepted 9 December 2022
Available online 27 December 2022

associated mainly with the interfacial connection between the filler and the EP, which resists deformation. Such nanosized fillers can reduce the stress and surface energy of the EP, improving the adhesion between the composite and fillers. Inorganic nanoparticles allow the deposition of inorganic films with optimal mechanical properties and reduce accumulated stress compared to neat films. Interfacial polymers with nanoscale fillers enable an increase in the interfacial area compared to that achieved in traditional composites.

Although the incorporation of inorganic nanoparticles improves the scratch resistance of polymers, the visible-light transparency of the EP coating is generally reduced. To overcome this effect, Wei et al. [7] presented a laminated SiO_2@TiO_2/ZnO coating where the ZnO exhibited a transmittance of 57.2 % in the visible region, suggesting that the ZnO nanofillers were not severely detrimental to the transparency of the coating. In addition, Song et al. [8,9] reported a transparent EP composite coating incorporating halloysite nanotubes; after Taber falling sand abrasion testing, the composite material continued to display reasonable light transmittance. Furthermore, after synthesizing ZrO_2 nanoparticles using a nonaqueous approach with benzyl alcohol as a coordinating solvent, Tao et al. [10] successfully prepared ZrO_2/epoxy nanocomposites with ZrO_2 contents as high as 50 wt%, displaying high optical transparency in the visible range. Despite these efforts, the fabrication of coatings with high scratch resistance and transmittance properties remains challenging because a trade-off exists between these two factors; a method for enhancing scratch resistance without sacrificing the transmittance properties is still lacking.

In this study, a novel, eco-friendly, and low-cost material namely, one-dimensional magnesium borate hydroxide, $xMgO{\cdot}yB_2O_3{\cdot}zH_2O$ (MBH) was employed to prepare EP/MBH nanocoatings, denoted as ExMBH (x = 1, 5, and 10 wt% MBH). The transparency and wear resistance of the neat and MBH-filled EP coatings were determined using optical transmittance and nanoscratch approaches, respectively. The morphology of the scratches was characterized by atomic force microscopy (AFM) and scanning electron microscopy (SEM) to investigate the deformation mechanisms after conducting the nanoscratch measurements. This study demonstrates coatings with enhanced scratch resistance without sacrificing high transparency.

2. Experimental procedures

2.1. Materials

Magnesium nitrate hexahydrate, $Mg(NO_3)_2{\cdot}6H_2O$, was purchased from Sinopharm Chemical Reagent Co., Ltd., China; boric acid (H_3BO_3), Tianjin Kemiou Chemical Reagent Co., Ltd., China; ammonium hydroxide ($NH_3{\cdot}H_2O$), Baiyin Liangyou Chemical Reagent Co., Ltd., China; the EP (Epoxy E44), Nantong Xingchen Synthetic Material Co., Ltd., China; and 4,4′-diaminodiphenylmethane (DDM), Shanghai Aladdin Bio-Chem Technology Co., Ltd., China.

2.2. Preparation of ExMBH (x = 0, 1, 5, and 10 wt% MBH) composite coatings

All reagents were of analytical grade and used without further purification. The products were synthesized using a modified hydrothermal reaction with $Mg(NO_3)_2{\cdot}6H_2O$, H_3BO_3, and $NH_3{\cdot}H_2O$ solutions in a molar ratio of 2:3:4. Following a standard procedure, 1 mol of $NH_3{\cdot}H_2O$ was added to a certain volume of H_2O and heated to 50 °C. Subsequently, 0.5 mol of $Mg(NO_3)_2{\cdot}6H_2O$, 0.75 mol of H_3BO_3, and 300 mL of H_2O were mixed with magnetic stirring for 30 min at 50 °C to obtain a homogeneous solution. The mixture was added dropwise to the $NH_3{\cdot}H_2O$ solution, and thereafter, the slurry was placed in a stainless steel autoclave (Multichem-600, Beijing Century Senlong Experimental Apparatus Co., Ltd.) at 190 °C for 10 h. Subsequently, the solution was allowed to cool to room temperature and then filtered, washed repeatedly with deionized water and ethanol, and dried at 100 °C for 8 h, yielding a white MBH powder.

To ensure good dispersion of the MBH nanorods in the EP matrix, the EP was heated in an oil bath at 90 °C until it melted, and the MBH was slowly added to the resin to form a mixture, which was subsequently stirred at 200 rpm using a magnetic mixer at 90 °C for 2 h. DDM (18 wt %) was added to the mixture and stirred continuously until it completely dissolved. Thereafter, the mixture was placed in a vacuum drying chamber at 100 °C for approximately 5 min and then poured into a mold to prepare the specimens, which were cured at 100 °C for 2 h and then at 150 °C for an additional 2 h. The pristine EP was also obtained using the same process for comparison.

2.3. Microstructural characterization and mechanical property testing

The structure of the composites was analyzed using an American PANalytical X'Pert Pro MPD X-ray diffractometer. K_α radiation (λ = 0.154 nm) generated from a Cu target was used as the diffraction source. The voltage and current parameters were 40 kV and 30 mA, respectively. The samples were coated with thin layers of gold, and the particle morphology and the fracture surfaces of the samples were characterized using a scanning electron microscope (Helios NanoLab 600i, FEI) at an accelerating voltage of 5 kV. Transmission electron microscopy (TEM) was conducted using a field-emission gun transmission electron microscope (Talos F200X, FEI) equipped with an energy-dispersive X-ray spectrometer (EDS) and operated at an accelerating voltage of 200 kV. The TEM samples were dispersed in acetone before observation, and the scanning transmission electron microscopy (STEM) mode was employed to analyze the elements and their distribution. Fourier transform infrared (FTIR) spectra of the samples were obtained from 4000 to 400 cm^{-1} using the KBr pellet technique with a Thermo Nicolet Nexus FTIR instrument (Thermo Fisher Nicolet 5700 spectrometer, USA). Raman spectra of the powder were acquired using a Thermo Scientific Raman instrument (Thermo Scientific DXR2, USA). The spectra were obtained using 532-nm laser light excitation over the wavenumber range of 100–6400 cm^{-1}. Thermogravimetric analysis (TGA) was performed from room temperature to 700 °C under a nitrogen atmosphere with a heating rate of 10 °C/min using a thermogravimetric analyzer (Q50, USA). The refractive index of the pure EP was evaluated using the oil immersion method at a constant temperature of 20 °C under a microscope (Ernst Leitz Wetzlar, Germany), with a transformer frequency of 50/60 Hz. The refractive index of the MBH powder was obtained by extrapolation using a single-cylinder Abbe refractometer (OPTON 11290, Germany). The transmittance and absorbance were measured using a UV–Vis spectrophotometer (TU-1810, Beijing). All samples were cleaned with ethanol, and five parallel samples were obtained from each specimen type. The Young's modulus was determined using a universal electromechanical testing machine (INSTRON 5966) under a maximum load of 2 kN, according to the ISO 527-2 standard, and the extension rate was 0.5 mm/min. Placed the samples in ultraviolet (UV) climate resistance test chamber (HJW/ZN-P-A, China), and treated them in accordance with GB/T 14522–2008, 24 h was selected as the common condition. The wavelength of UV light was 280–340 nm and the radiation intensity of the sample surface was 0.89 W/m^2.

The nanomechanical measurements of the EP and EP/MBH nanocomposites were performed by nanoscratch testing using a Hysitron TI 950 TriboIndenter. A spherical diamond tip with a 10 μm radius was used as the indenter probe. The nanoscratch tests involved making scratches 250 μm in length using a constant normal force (F_n) at different loads (5, 10, 30, and 50 mN). As shown in Fig. 1(a) and (b), each scratching procedure comprises three steps. First, a prescan with a constant normal force of 2 mN was performed to obtain the initial surface information (height and roughness) of the tested sample, which could then be used to correct the final penetration depth (P_d) and residual depth (R_d; i.e., the tilt correction). The tip was subsequently turned back and was allowed to scratch the composites at a rate of 0.5 mm/s, with the normal load increasing uniformly while maintaining a

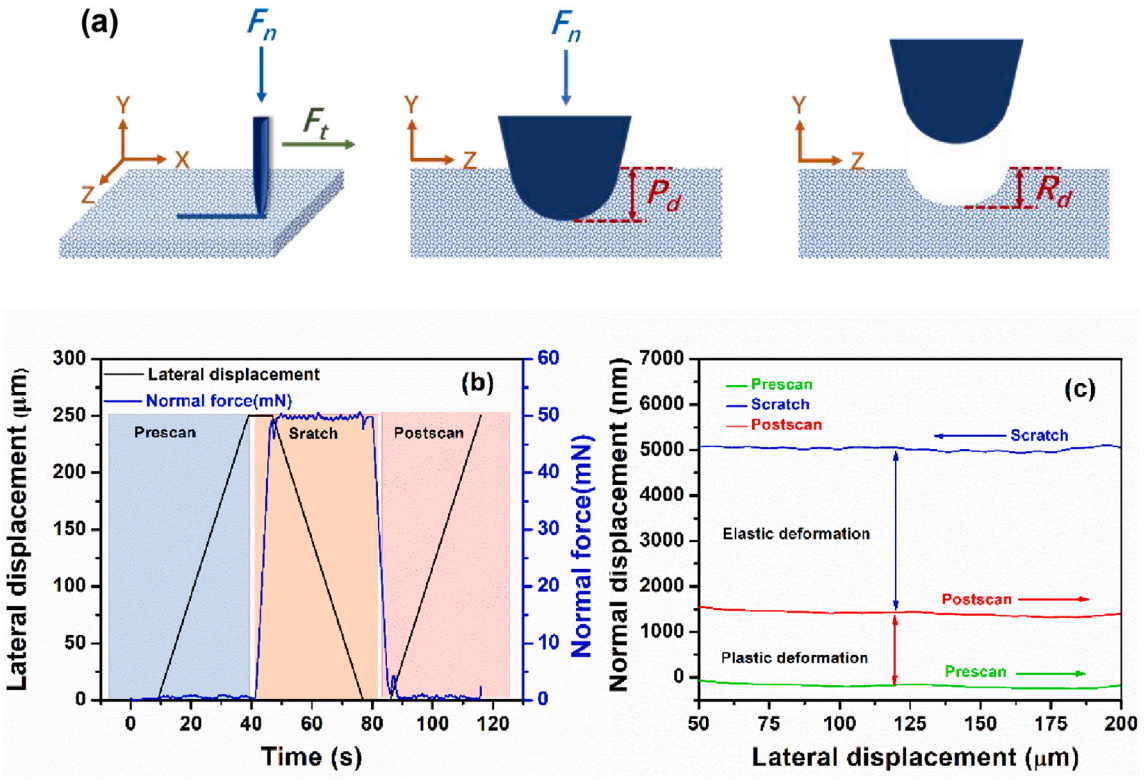

Fig. 1. (a) Schematic representation of nanoscratch tests on the surface of the samples, where F_n and F_t are the normal and tangential loads, respectively; (b) load function of the nanoscratch test under the constant load of 50 mN; and (c) representative nanoscratch curves corresponding to the three scratch stages – prescan, scratch, and postscan.

constant load (e.g., 50 mN). Finally, a postscan of the tip with a normal force of 2 mN was performed to obtain the residual depth information of the scratch [11]. The arrows in Fig. 1(c) indicate the scanning directions during the experiment (left to right for the pre and postscans, and right to left for the scratch stage). The difference between the height profiles of the pre and postscans indicates the permanent residual deformation caused by the scratch, corresponding to R_d in Fig. 1(a). Additionally, the difference between the height profiles obtained during the scratching and postscan stages was due to elastic recovery. The elastic and plastic deformations can be derived from P_d and the total normal displacement, as shown schematically in Fig. 1(a). The two significant parameters, the scratch recovery index (β_s) and the plastic energy (P_e), were evaluated using Eqs. (1) and (2), respectively [12]:

$$\beta_s = \frac{P_d - R_d}{P_d} \tag{1}$$

$$P_e = R_d \times F_n \tag{2}$$

where P_d is the penetration depth, R_d is the residual depth, and F_n is the normal force.

The scratch tracks on the samples were analyzed to determine the widths of the scratches, and their average values (b) were used to calculate the scratch hardness (H_s) using Eq. (3):

$$H_s = \frac{8F_n}{\pi b^2} \tag{3}$$

The topography of the scratches was characterized using a Park AFM instrument.

3. Results and discussion

3.1. Characterization of MBH

As shown in Fig. 2, the phase composition and structure of MBH were examined by X-ray diffraction (XRD), and all the diffraction peaks can be indexed as MBH (PDF No. 01-070-1762) [13]. The XRD spectrum reveals only the MBH crystalline structure, without other detectable peaks, indicating perfect crystal growth [14].

The morphology and size of MBH were characterized using SEM and TEM. The product exhibits typical nanorod morphology with lengths of

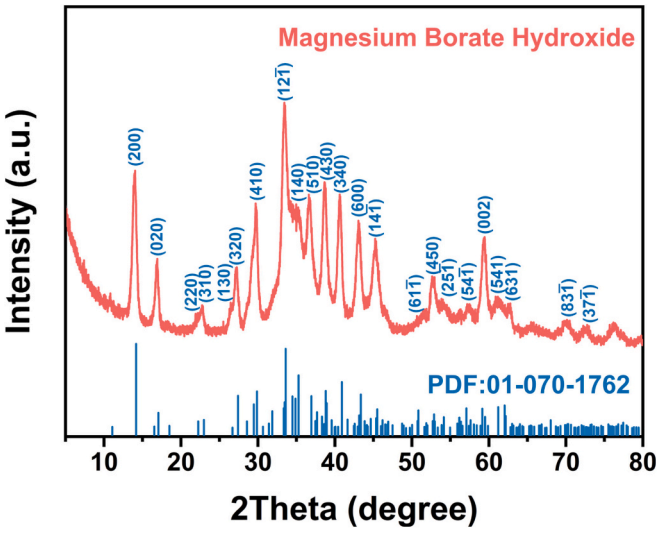

Fig. 2. A representative XRD spectrum of MBH.

approximately 500–800 nm and widths of approximately 30 nm, as shown in the SEM image in Fig. 3(a). Representative TEM and selected area electron diffraction (SAED) images in Fig. 3(b) and (c) illustrate the crystalline structure of MBH and the corresponding SAED pattern. The constituent elements were confirmed by TEM, as shown in Fig. 3(d), indicating that the sample is mainly composed of Mg, B, and O, as shown in Fig. 3(e)~(g).

The FTIR and Raman spectra of MBH are shown in Fig. 4(a) and (b), respectively. In Fig. 4(a), the typical O—H stretching, H-O-H bending, $B_{(3)}$-O antisymmetric stretching, B-O-H in-plane bending, $B_{(3)}$-O outside bending, $B_{(4)}$-O antisymmetric stretching, and Mg—O stretching vibrations can be observed in the FTIR spectrum [14–17]. In Fig. 4(b), the strong peaks at 3965 and 3564 cm^{-1} represent the O—H stretching vibrations; the $B_{(4)}$-O antisymmetric stretching is detected at 1060 cm^{-1}; the peaks at 833 and 319 cm^{-1} are the symmetric and antisymmetric stretching vibrations of $B_{(4)}$-O, respectively; and the peak at 612 cm^{-1} corresponds to the symmetric stretching of $B_{(3)}$-O [15,18]. These results are consistent with the XRD and chemical analysis in Figs. 2 and 3, which illustrates that the vibrational modes of Mg—O, B—O, B-O-H, and H-O-H are detectable. Additionally, the FTIR and Raman spectroscopy results verify that MBH was successfully prepared.

To determine the composition, a sample was weighed, dissolved in nitric acid, and transferred to a 100-mL volumetric flask. The magnesium ion content was determined using the EDTA method, and the total boron content (represented by B_2O_3) was measured using the mannitol method [17,19]. The specimens are composed of 42.58 % MgO, 41.61 % B_2O_3, and H_2O according to the MgO:B_2O_3:H_2O mole ratio of 1.06: 0.60: 0.88. The thermal stability results show that the total weight loss is 14.57 % from 50 to 550 °C, as presented in the TGA curve in Fig. 5. This corresponds to a loss of 1.5 water molecules compared with the initial value of 14.42 %, indicating that the chemical formula for this product is $2MgO{\cdot}B_2O_3{\cdot}1.5H_2O$.

3.2. Transparency of the EP and its nanocomposites

Optical transparency is of great importance for applications in the field of encapsulation materials in the visible range [20]. The transparencies of the 1 mm-thick EP and EP/MBH nanocoatings after double-sided polishing are shown in Fig. 6; double-sided polishing provides a more practical reference value compared to single-sided polishing [21]. In the visible region, all patterns could be observed in these samples, indicating high transparency for all the synthesized ExMBH (x = 1, 5, and 10 wt% MBH) nanocoatings. Only a minor effect on transparency was observed for an increase in the amount of MBH up to 10 wt%.

To further examine the impact of MBH on the optical properties of the composites, the optical transmittance of the EP/MBH nanocoatings was measured in the visible and UV wavelength range of 200–800 nm. Fig. 7 depicts the transmittance spectra of the 1 mm-thick EP/MBH nanocoatings with different MBH loadings after double-sided polishing. In Fig. 7(a), the cured epoxy shows a transparency of 90 % in the visible region and a sharp UV cutoff at 350 nm [10]. Above 400 nm, with increasing MBH content in the neat EP, the EP/MBH nanocoatings continue to display high transparency; even at a concentration of 10 wt %, a transparency of more than 85 % is maintained in the visible region. ExMBH shows a low transmittance in the UV region due to its UV absorption capacity. One reason for the high transparency of nanocoatings is the refractive index matching between the epoxy matrix and MBH [22,23]; the refractive indices of neat EP (1.61) and MBH (1.64) correspond to this observation [21]. After the incorporation of MBH, the nanocoatings maintained excellent optical transmittance. However, compared with that of the neat EP, the transmittance of E10MBH decreased by approximately 6 %. According to Rayleigh's scattering law,

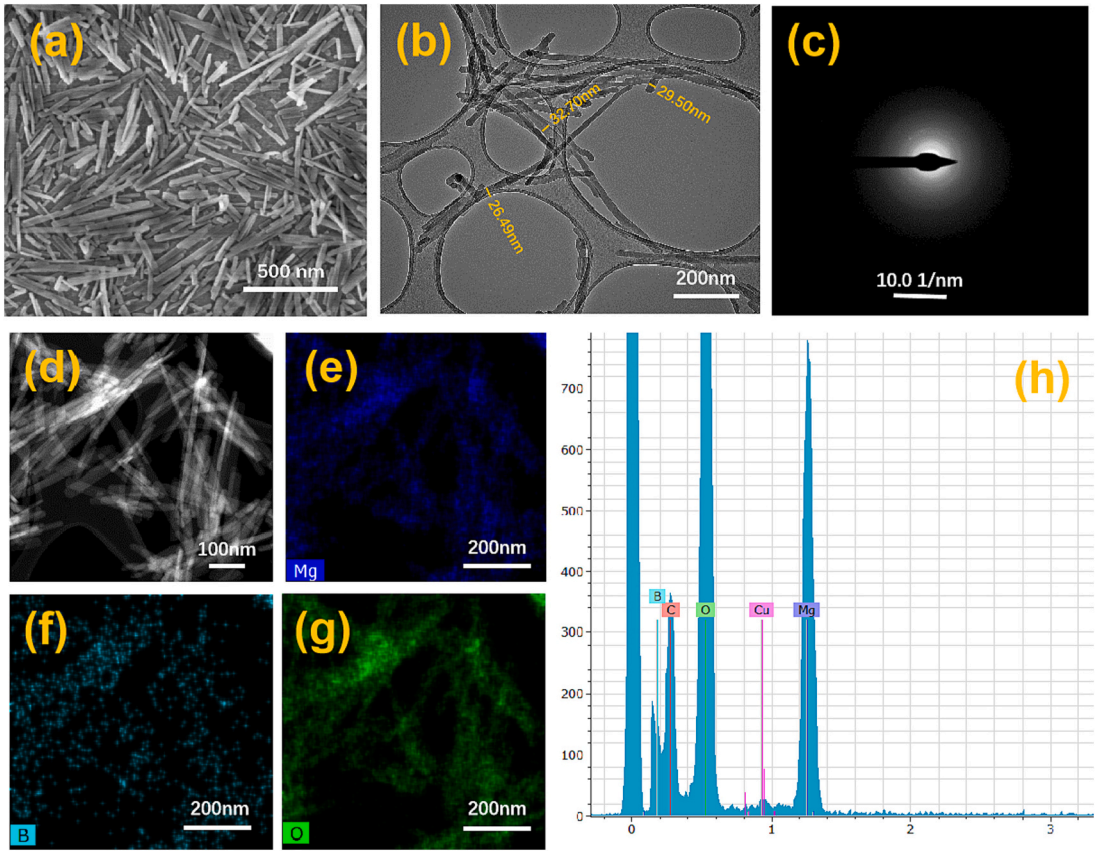

Fig. 3. (a) SEM images of MBH morphology; (b) TEM images of MBH and (c) its corresponding SAED pattern; (d) HAADF-STEM image and (e) STEM-EDX mapping of Mg, (f) B, and (g) O; and (h) the elemental EDS spectrum of MBH.

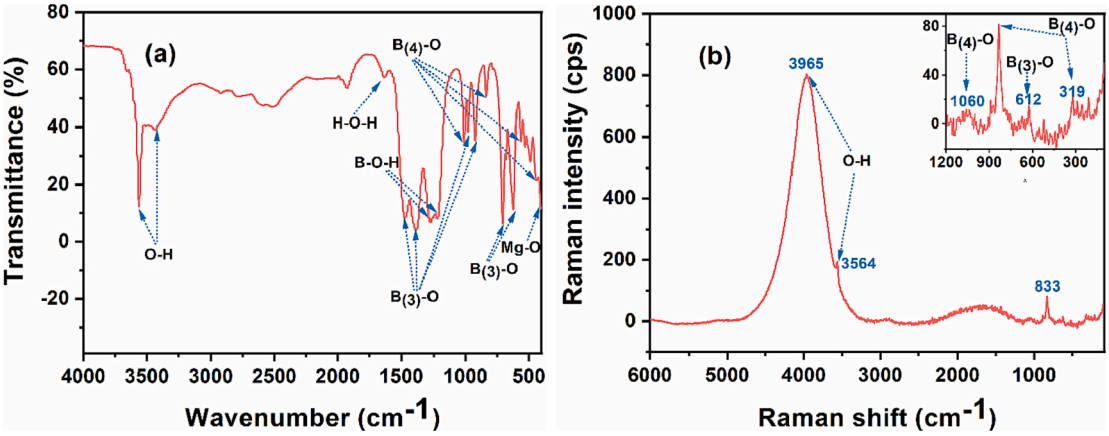

Fig. 4. (a) FTIR and (b) Raman spectra of MBH.

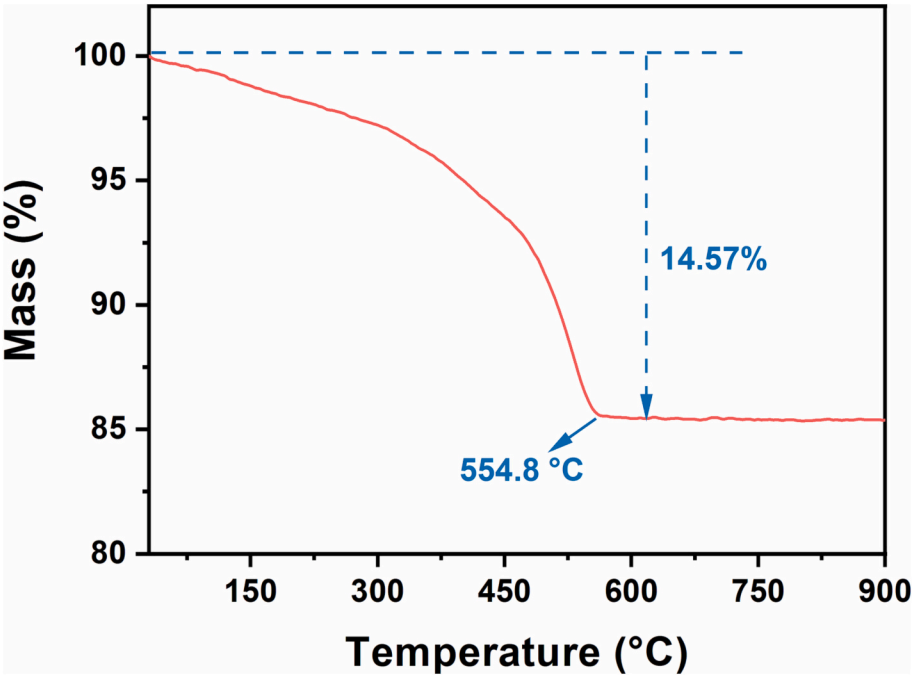

Fig. 5. TGA curve of MBH.

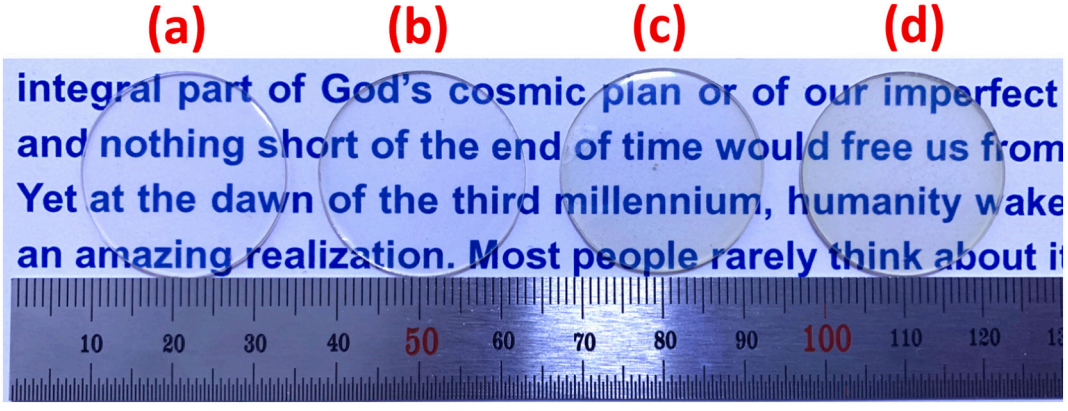

Fig. 6. Digital photos of the neat EP and nanocomposites: (a) neat EP (E0MBH), (b) E1MBH, (c) E5MBH, and (d) E10MBH.

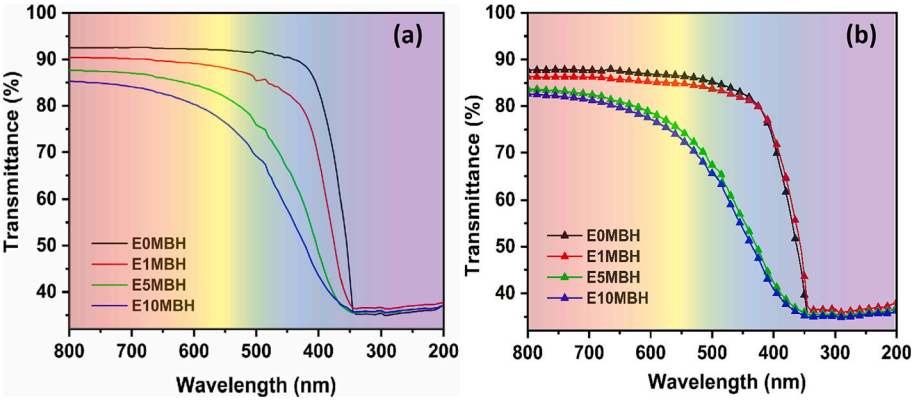

Fig. 7. Transmittances of the neat EP and EP/MBH nanocomposites (a) before and (b) after UV aging.

the volume fraction and average radius of particles play important roles in determining the optical transmittance [10,23]. Previous studies have shown that dispersion and particle size have a significant impact on the transparency of nanocomposites [24–26]. Proceed from the practical anale, the UV aging behaviors of EP/MBH nanocoatings are shown in Fig. 7(b). For pure EP, the transparency lost by 4.8 % after 24 h of irradiation, while ExMBH lost slowly. Comparing the aging performance of pure EP, it could be observed that ExMBH exhibit a stable transparency performance after the UV irradiation. Clearly, the ExMBH possess obvious advantages against the UV irradiation compared to pure EP.

To further investigate the dispersion of MBH in the EP, SEM images of brittle fracture sections were obtained, as presented in Fig. 8(a)~(d). After MBH was added to the EP matrix, part of it was evenly dispersed in the composites. Notably, the remainder of the MBH also exhibited even dispersion by forming tiny agglomerates and bundles (marked by the orange arrows). Redundant interfaces arise in MBH and EP with the increasing MBH concentration per unit area, which refract incident light multiple times and cause the light transmittance to gradually decrease.

3.3. The mechanical properties of the neat EP and EP/MBH composites

The effect of MBH on the dynamic mechanical properties of the neat EP and EP nanocomposites was evaluated using a dynamic mechanical analyzer. Fig. 9(a) plots the storage modulus as a function of the temperature for the neat EP and ExMBH (x = 1, 5, and 10 wt% MBH) nanocomposites. The curves include three stages: the primary (40–140 °C), secondary (140–160 °C), and tertiary steady states. In the

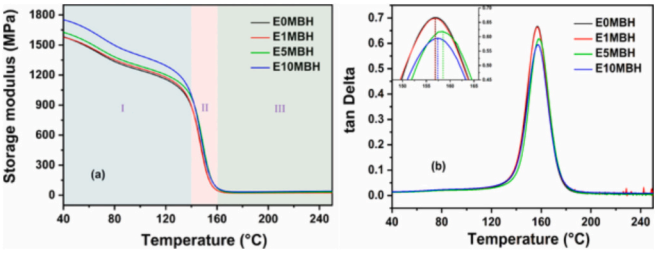

Fig. 9. (a) Dynamic mechanical and (b) thermal behavior analysis of the neat EP and EP/MBH nanocomposites.

primary stage, the storage modulus of ExMBH changes slightly, increasing from 1582 to 1752 MPa with the addition of 10 wt% MBH. Moreover, the storage modulus of the ExMBH nanocomposites gradually decreases as the temperature increases. In the secondary stage, the values of the storage modulus of both the EP and ExMBH composites are similar and rapidly decrease as the temperature increases, reaching approximately 0 MPa at 160 °C. Fig. 9(b) plots tan δ versus temperature for the neat EP and EP/MBH nanocomposites to indicate the glass transition temperature (T_g), determined from the peak of the curve. Compared to that of the neat EP, the T_g values of ExMBH are slightly increased. This occurs because the diffusion rate of one-dimensional MBH limits the relative relaxation of the polymeric segment at the T_g, and the transition from the rubber state to the glass state is stymied [27,28].

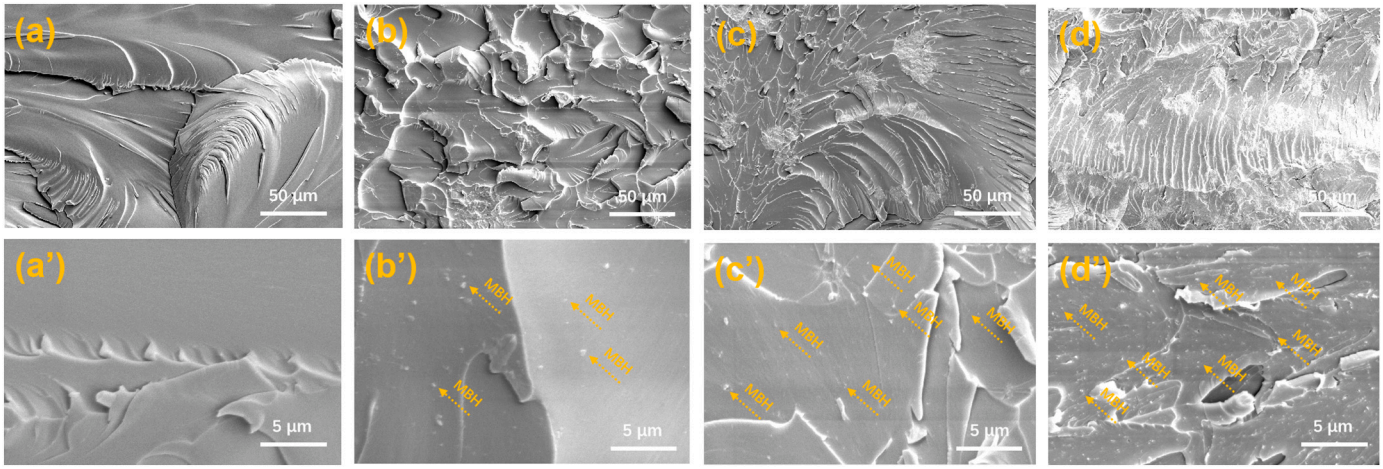

Fig. 8. SEM images of the sample: (a) and (a') E0MBH, (b) and (b') E1MBH, (c) and (c') E5MBH, and (d) and (d') E10MBH. The orange arrows indicate the MBH nanocomposite fillers in the EP.

Nanoscratch tests with a normal load, F_n (5, 10, 30, and 50 mN), were performed on the neat EP and ExMBH nanocomposites to elucidate the effect of the MBH nanofillers on scratching resistance. According to the scratch curves, the recovery depth (R_d) and penetration depth (P_d) were determined using the methods described in Fig. 1(a). The variations in the scratch depth (after the tilt correction) are plotted as a function of the lateral displacement at a normal load of 5 mN, as shown in Fig. 10. The representative scratch curves comprise three stages: the prescan, scratch, and postscan stages. The average normal displacement was determined for lateral displacements ranging from 50 to 200 μm. The fluctuations in the E10MBH composite indicate that the addition of 10 wt% MBH increases the friction between the tip and the sample.

The average depth values provide acceptable accuracy and reproducibility. Fig. 10(a) shows a total scratch depth (P_d) of 560 nm, of which only ~380 nm is elastically recovered (R_d), leaving a residual scratch depth of 180 nm when the normal load is released. In Fig. 10(b) ~(d), the residual scratch depths of E1MBH, E5MBH, and E10MBH are 129 ± 6.5, 55 ± 26, and 14 ± 8 nm, respectively, which are less than those in the neat EP samples. This suggests that the samples with 1, 5, and 10 wt% MBH show substantially enhanced scratch resistance and less plastic deformation displacement. Moreover, the normal displacements in the pre and postscan stages overlap closely, indicating that the surface suffers no plastic deformation under the load of 5 mN. Therefore, the recovery ability and wear resistance of the EP/MBH composites are significantly enhanced compared to those of the neat EP. Comparable results are obtained for the neat EP and EP/MBH composites under a normal load of 30 mN (Fig. S1, Supporting Information). To illustrate the scratch morphology, the scratched surfaces of the neat EP and EP/MBH composites were examined. From Fig. 11, the scratch morphologies reveal that the recovery displacement after scratching decreases as the wt% of the MBH increases. Meanwhile, the ExMBH composites require more energy to deform, in agreement with the increased T_g values in Fig. 9.

To qualify the scratch properties of these composites, the recovery index (β_s) and plastic energy (P_e) parameters were obtained according to Eqs. (1) and (2), respectively. In Fig. 12(a), β_s increases to 0.72 ± 0.02, 0.92 ± 0.04, and 0.98 ± 0.01 with the addition of 1, 5, and 10 wt% MBH, respectively. The β_s indices are enhanced by 12.5, 43.8, and 53.0 % compared to that of E0MBH (0.64 ± 0.03) under a load of 5 mN. In addition, the opposite trend is observed for β_sE0MBH with the maximum P_e, whereas E10MBH exhibits the lowest value at all indentation load variations in Fig. 12(b). The scratch hardness (H_s) in Fig. 12(c) is another parameter for evaluating the scratch resistance and was calculated based on Eq. (3). The width of each scratch was determined using AFM topography images, as shown in Figs. S2 and S3 in the Supporting Information. A noticeable enhancement in H_s, namely, the wear resistance, is observed with the addition of MBH at loads of less than 30 mN. For instance, under a load of 10 mN, the lowest H_s value is obtained for E0MBH, which is improved by ~9, ~18, and ~21 % after the incorporation of 1, 5, and 10 wt% MBH, respectively. This suggests that the enhanced scratch resistance in the EP coating is induced by the MBH nanofiller, as shown in Fig. 12(d). To eliminate the size effect, the

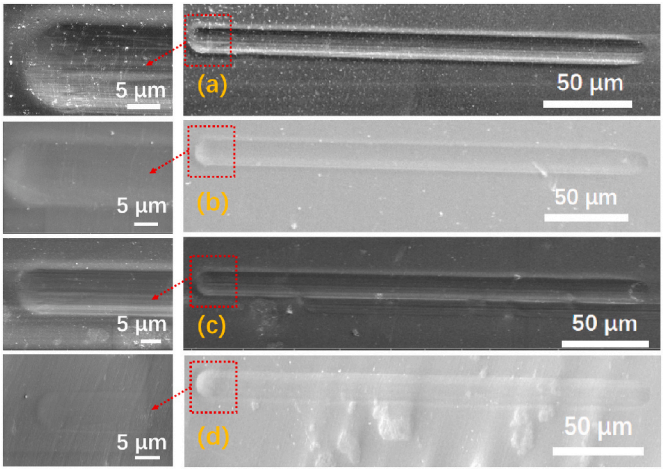

Fig. 11. SEM images of the scratch morphologies in the neat EP and EP/MBH composites under a normal load of 30 mN: (a) E0MBH, (b) E1MBH, (c) E5MBH, and (d) E10MBH.

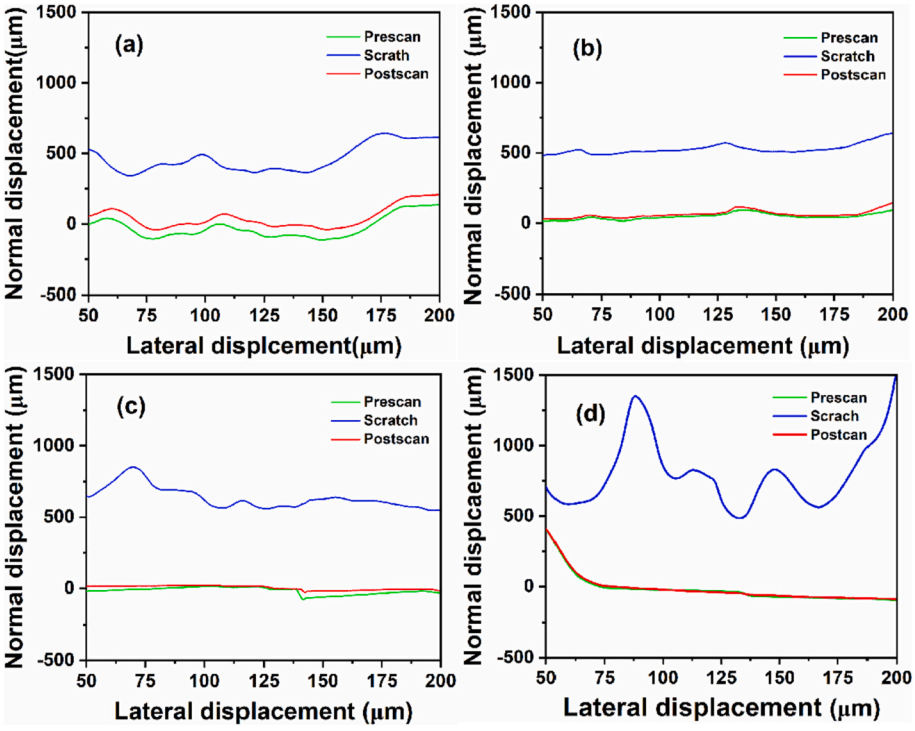

Fig. 10. Scratch curves at a load of 5 mN: (a) E0MBH, (b) E1MBH, (c) E5MBH, and (d) E10MBH. P_d represents the penetration depth and R_d is the recovery depth.

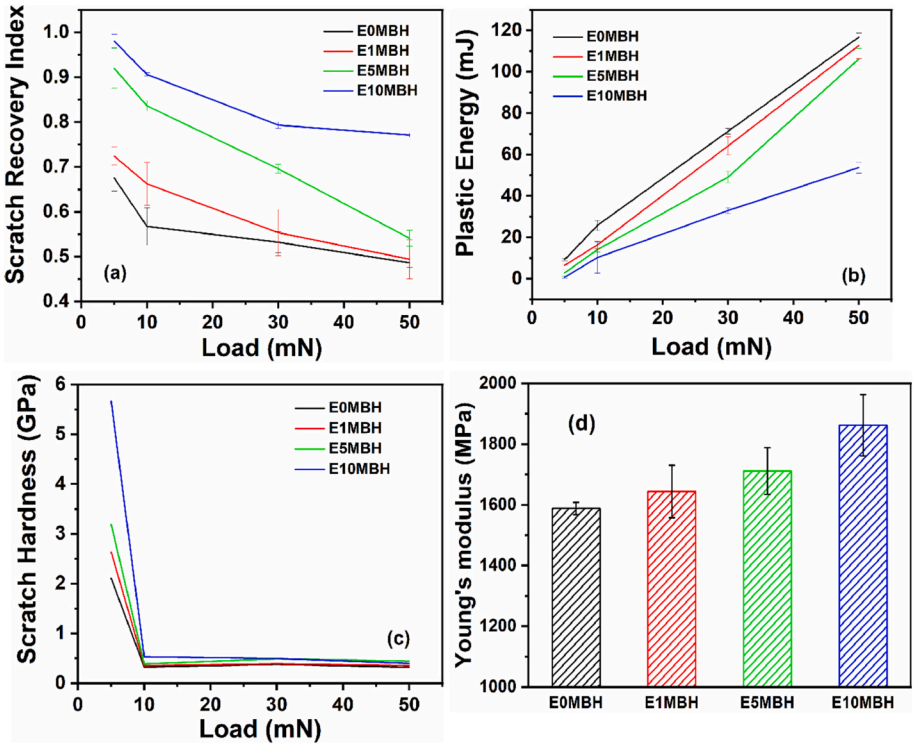

Fig. 12. Variation of the (a) scratch recovery index, (b) plastic energy, and (c) scratch hardness of the EP/MBH composites with respect to the load; and (d) the Young's moduli of the EP/MBH samples.

difference between the neat EP and EP/MBH scratch mechanisms under a load of 30 mN, rather than 10 mN, is considered in the following discussion.

The surface morphologies of the scratched samples under a normal loading of 30 mN were characterized using AFM 3D imaging, as presented in Fig. 13. The topography close to the end of the scratch displays the distinctive plowing and plastic deformation in the EP without MBH fillers. The scratch sliding surface in the EP is rougher than that in the MBH-filled materials, as shown in Fig. 13(b)~(d). Because the neat EP coating is fragile to the extent that it can crack and break away from the surface of the specimen, as compared to the case for the MBH-filled composites, a more distinctive piling-up area appears along the tracks in the EP. The EP/MBH composites exhibit a relatively smooth surface upon scratching, which further confirms their higher abrasion wear resistance, as shown in the red regions in Fig. 13(a). The corresponding wear depths around the scratch for the neat EP and EP/MBH composites are 1.4 and 0.6 μm, respectively, as illustrated in Fig. 13(e). The results reveal a larger pile-up region along the scratch track in the EP sample. The wear of the bulk material plowing regions is generally dependent on the presence of fillers in the EP, which can significantly affect the shear strength of the sliding interface [29]. An increase in the contact shear strength owing to the modified modulus of EP/MBH composites can notably enhance wear resistance by amplifying the stress. Moreover, as shown earlier in Fig. 1(a), the penetration depth and scratch resistance depend on the normal force (F_n) and resistance to the tangential force (F_t) during the sliding process. This induces different stress fields, including compressive stress in front of and tensile stress behind the indenter tip. For all the composites, the matrix beneath the indenter is

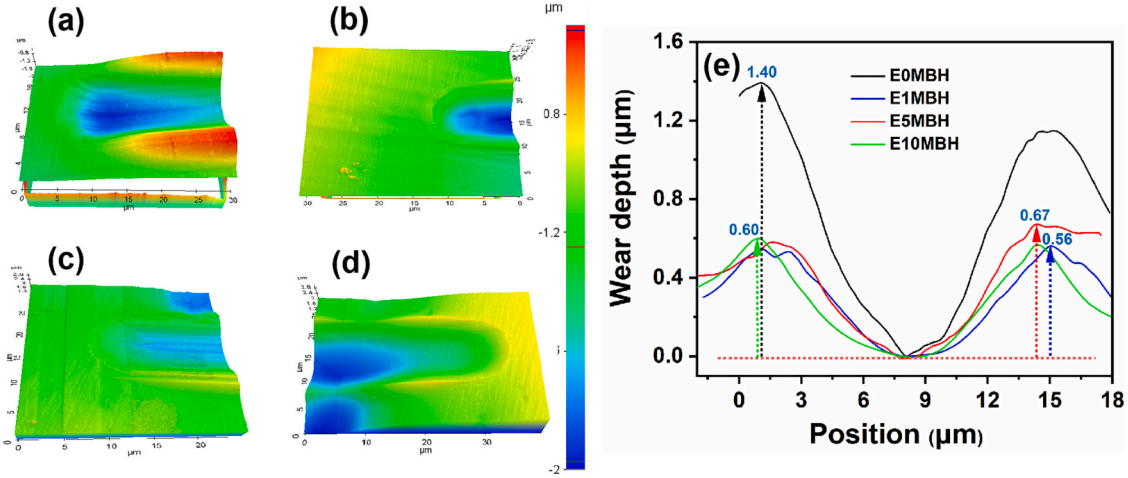

Fig. 13. Topography of the end of the scratch for (a) E0MBH, (b) E1MBH, (c) E5MBH, and (d) E10MBH at a load of 30 mN; and (e) the wear depth of the EP/MBH composites.

expected to show both viscoelastic and viscoplastic deformation because of the difference in the stress field [12]. During the scratch process, the plastic energy is associated with the plowing region. Elastic energy is released in the form of thermal energy and results in frictional heating, which can be absorbed by the composites. Energy is absorbed by the matrix instead of inducing more plastic deformation, which helps explain the lower pile-up region and smoother slide trace for the MBH-filled composites.

As shown in Fig. 14(a)–(f), shear stress is applied only to break the C—C bonds in the EP. In the EP/MBH composites, the chains between the EP and MBH interfaces can fracture as the elastic energy is increased. This mechanism indicates that chain scission is favorable in EP/MBH composites, leading to a much smoother scratch [30]. Studies have reported that the improvement in the wear performance of polytetrafluoroethylene is ascribed to certain inorganic particles modified by carboxylate end-group bonds. Therefore, the reinforced tribofilms possess robust sliding surfaces, giving rise to a significant reduction in wear resistance [31,32]. In nanocrystalline metals, high thermal stability is associated with low wear properties [29]. The thermomechanical stability of materials can mitigate the stress-driven microstructural evolution at elevated contact stresses and, ultimately, suppress delamination wear.

Furthermore, incorporating inorganic fillers, such as nanoscale ZnO, Al_2O_3, MgO, and B_2O_3, into composites can effectively decrease the wear rate [33–36]. The wear mechanisms are related to the destruction of the banded structure of the matrix and the physical interactions at the polymer/filler interface. Herein, the possible reasons for the enhanced wear resistance are associated with the higher crosslinking density, which is influenced by the distribution of the chain-like structure and shape of the MBH nanofillers. The proposed recovery mechanism is attributed to the effect of one-dimensional MBH nanorods interconnecting to form a three-dimensional network, as illustrated in Fig. 14. The dispersion of MBH in the EP matrix can release the stress concentration when the tip scratches the surface of the specimen [29]. A few researchers have postulated that the enhancement in material yield strength and elastic modulus can allow the material to resist scratching by plastic deformation and plowing along the scratch track [9]. Hence, nanoparticle-filled composites and transfer film generation can enhance scratch resistance.

4. Conclusions

In summary, one-dimensional MBH was successfully synthesized using a simple method and employed as a filler in an EP to balance its mechanical durability and optical properties. The roles of the MBH fillers in the transparency and nanoscratch properties of the neat EP and ExMBH (x = 1, 5, and 10 wt% MBH) composite coatings were investigated. E10MBH exhibits the highest scratch resistance and maintains a transmittance of over 85 %. The significantly improved wear resistance can be attributed to the uniform dispersion of MBH in the polymer matrix, in addition to the interfacial properties, higher crosslinking density, and nanoparticle network, which are influenced by the one-dimensional shape and structure of the MBH nanofillers. The refractive index matching between the EP and MBH and the dispersion of the particles play key roles in the transmittance of the nanocomposite. As a representative of eco-friendly and novel inorganic materials, MBH

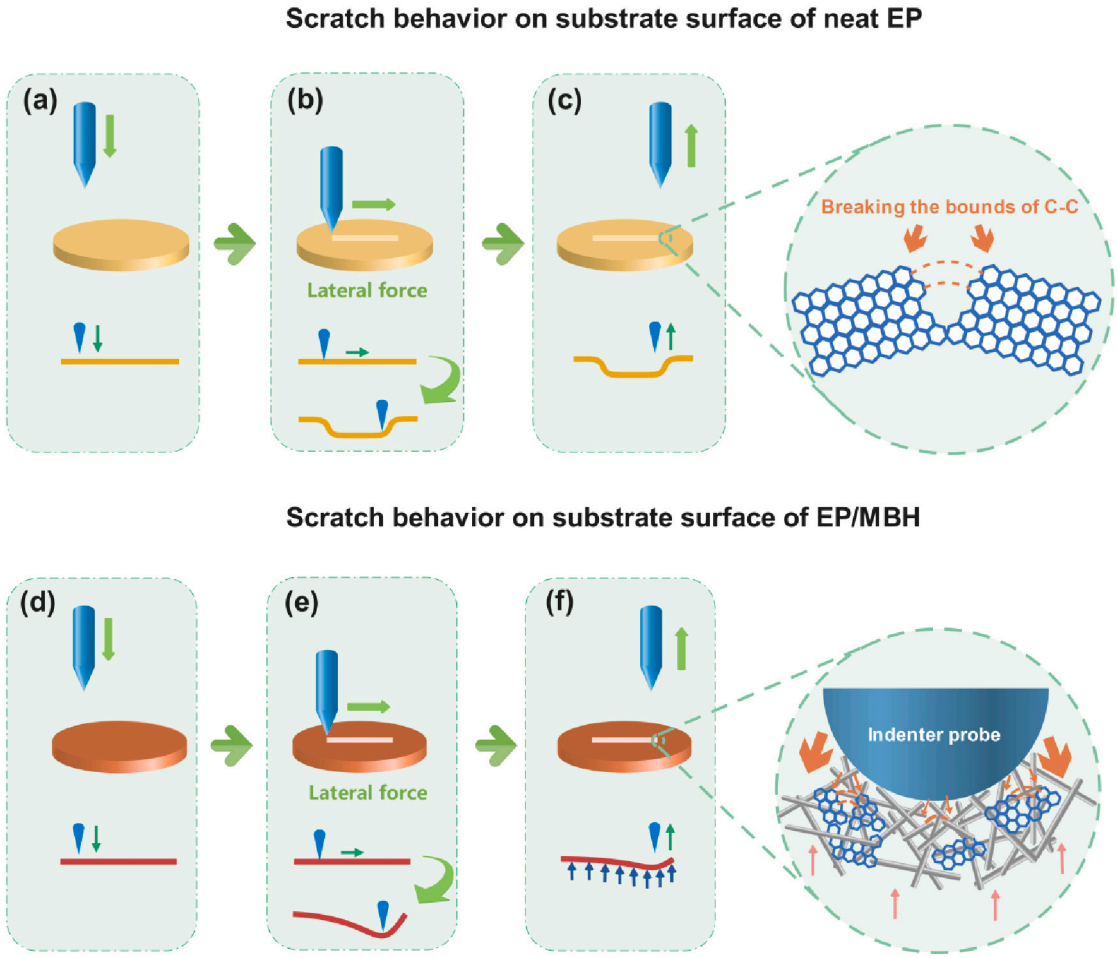

Fig. 14. (a) to (f) Schematic illustration of the mechanism of the nanoscratch technique using a nano-indenter. The inset figures depict the debonding in the films.

demonstrates strong potential for various applications, including light-emitting diodes, solar cells, and coatings.

CRediT authorship contribution statement

Na Li: Conceptualization, Methodology, Formal analysis, Writing-Original draft.

Na Li: Methodology, Validation, Writing–Review & Editing.

Zhi-qi Liu: Conceptualization, Funding acquisition, Project administration.

Yun-xian Yang: Investigation, Validation, Resources.

Yong-cang Ying: Methodology, Formal analysis, Investigation.

Zi-yuan Zhou: Investigation.

All authors contributed to drafting of the manuscript. The manuscript is approved by all authors for publication.

Declaration of competing interest

We declare that we have no financial and personal relationships with other people or organizations that can inappropriately influence our work, there is no professional or other personal interest of any nature or kind in any product, service and company that could be construed as influencing the position presented in, or the review of, the manuscript entitled “Enhanced Wear Resistance and Transparency of Epoxy Resin Coatings Filled with Novel One-dimensional Magnesium Borate Hydroxide Nanorods” (ID PROC-D-22-01337).

Data availability

Data will be made available on request.

Acknowledgements

This research was partly funded the Natural Science Foundation of China (U1607104), Ministry of Industry and Information Technology of China (P173008047). Anhui University (Talent Fund−China S020318008/001).

Appendix A. Supplementary data

Supplementary data to this article can be found online at https://doi.org/10.1016/j.porgcoat.2022.107370.

References

[1] Y. Li, L. Zhang, C. Li, Highly transparent and scratch resistant polysiloxane coatings containing silica nanoparticles, J. Colloid Interface Sci. 559 (2019).
[2] F. Guo, Y. Zhang, L. Cai, L. Li, NiFe prussian blue analogue nanocages decorated magnesium hydroxide rod for enhancing fire safety and mechanical properties of epoxy resin, Compos. Part B 233 (2022), 109650.
[3] H. Teisala, P. Baumli, S.A.L. Weber, D. Vollmer, H.-J. Butt, Grafting silicone at room temperature—a transparent, scratch-resistant nonstick molecular coating, Langmuir 36 (16) (2020) 4416–4431.
[4] Z. Hang, B. Zza, D. Jq, A. Pc, C. Wsab, Defect engineering of carbon nanotubes and its effect on mechanical properties of carbon nanotubes/polymer nanocomposites: a molecular dynamics study, <sb:contribution><sb:title>Compos. </sb:title></sb:contribution><sb:host><sb:issue><sb:series><sb:title>Commun.</sb:title></sb:series></sb:issue></sb:host> (2021) 28.
[5] H. Pelletier, C. Mendibide, A. Riche, Mechanical characterization of polymeric films using depth-sensing instrument: correlation between viscoelastic-plastic properties and scratch resistance, Prog.Org.Coat. 62 (2) (2008) 162–178.
[6] C. Cazan, A. Enesca, L. Andronic, Synergic effect of TiO_2 filler on the mechanical properties of polymer nanocomposites, Polymers 13 (12) (2021) 2017.
[7] G. Wei, D. Yang, T. Zhang, X. Yue, F. Qiu, Fabrication of multifunctional coating with high luminous transmittance, self-cleaning and radiative cooling performances for energy-efficient windows, Sol. Energy Mater. Sol. Cells 202 (2019), 110125.
[8] K. Song, R. Polak, D. Chen, M.F. Rubner, R.E. Cohen, K.A. Askar, Spray-coated halloysite-epoxy composites: a means to create mechanically robust, vertically aligned nanotube composites, ACS Appl. Mater. Interfaces 8 (31) (2016) 20396–20406.
[9] K. Song, D. Chen, R. Polak, M.F. Rubner, R.E. Cohen, K.A. Askar, Enhanced wear resistance of transparent epoxy composite coatings with vertically aligned halloysite nanotubes, ACS Appl. Mater. Interfaces 8 (51) (2016) 35552–35564.
[10] P. Tao, Y. Li, R.W. Siegel, L.S. Schadler, Transparent dispensible high-refractive index ZrO_2/epoxy nanocomposites for LED encapsulation, J. Appl. Polym. Sci. 130 (5) (2013) 3785–3793.
[11] I. Navarro-Baena, A. Jacobo-Martín, J.J. Hernández, J.R. Castro Smirnov, F. Viela, M.A. Monclús, M.R. Osorio, J.M. Molina-Aldareguia, I. Rodríguez, Single-imprint moth-eye anti-reflective and self-cleaning film with enhanced resistance, Nanoscale 10 (33) (2018) 15496–15504.
[12] S. Das, S. Halder, A. Sinha, M.A. Imam, N.I. Khan, Assessing nanoscratch behavior of epoxy nanocomposite toughened with silanized fullerene, ACS Appl.Nano Mater. 1 (7) (2018) 3653–3662.
[13] Y.-Q. Ma, L. Zhang, Z.-H. Liu, In situ preparation and formation mechanism of $2MgO{\cdot}B_2O_3{\cdot}1.5H_2O$–$Mg(OH)_2$ nanocomposite and its synergistic flame retardancy, J. Therm. Anal. Calorim. 132 (1) (2018) 59–64.
[14] A.-M. Chen, J. Li, P. Gu, J. Hu, A facile route for the flowerlike $Mg_7B_4O_{13}{\cdot}7H_2O$ nanostuctures: synthesis, growth mechanism and thermal treatment, Powder Technol. 267 (2014) 54–60.
[15] E.M. Derun, A.S. Kipcak, F.T. Senberber, M.S. Yilmaz, Characterization and thermal dehydration kinetics of admontite mineral hydrothermally synthesized from magnesium oxide and boric acid precursor, Res. Chem. Intermed. 41 (2) (2015) 853–866.
[16] Z.-H. Liu, S.-Y. Gao, M.-C. Hu, S.-P. Xia, Synthesis and thermodynamic properties of $MgO{\cdot}B_2O_3{\cdot}4H_2O$, Chin. J. Chem. 20 (12) (2002) 1519–1522.
[17] L. Zhang, Z.-H. Liu, Preparation of $2MgO{\cdot}B_2O_3{\cdot}1.5H_2O$ nanomaterials and evaluation of their flame retardant properties by a thermal decomposition kinetic method, J. Therm. Anal. Calorim. 129 (2) (2017) 715–719.
[18] Z.-H. Liu, M.-C. Hu, S.-Y. Gao, Synthesis, characterization and solution Raman spectroscopic analysis of MgO.3B2O3.3.5H2O. <sb:contribution><sb:title><sb:maintitle>Chin.</sb:maintitle> </sb:title></sb:contribution><sb:host><sb:issue><sb:series><sb:title>J. Inorg. Chem.</sb:title></sb:series></sb:issue></sb:host> 18 (12) (2002) 1226–1228.
[19] H. Wang, L. Li, M. Wang, X. Lei, Y. Guo, T. Deng, Solid-liquid phase equilibria of the aqueous ternary system ($MgSO_4 + Mg_2B_6O_{11} + H_2O$) at (288.15, 298.15, and 308.15) K, J. Chem. Eng. Data 62 (10) (2017) 3334–3340.
[20] D.J. Kang, G.U. Park, H.Y. Park, H.-G. Im, A robust transparent encapsulation material: silica nanoparticle-embedded epoxy hybrid nanocomposite, Compos. Sci. Technol. 144 (2017) 107–113.
[21] Z.Q. Liu, N. Li, F. Guo, Y.C. Jia, L.J. Li, Preparation and fire - safety performance of transparent epoxy resin/basic magnesium borate composite, J.Salt Lake Res. 27 (4) (2019).
[22] W.T. Schaller, A.C. Vlisidis, M.E. Mrose, Macallisterite, $2MgO{\cdot}6B_2O_3{\cdot}15H_2O$, a new hydrous magnesium borate mineral from the Death Valley region, Inyo County, California1, Am. Mineral. 50 (5–6) (1965) 629–640.
[23] Y. Kagawa, H. Iba, M. Tanaka, H. Sato, T. Chang, Fabrication and optical/thermal properties of glass particle–epoxy optically transparent composites, Acta Mater. 46 (1) (1998) 265–271.
[24] Y.M. Deng, A.J. Gu, Z.P. Fang, The effect of morphology on the optical properties of transparent epoxy/montmorillonite composites, Polym. Int. 53 (1) (2004) 85–91.
[25] C. Liu, T. Chen, C.H. Yuan, C.F. Song, Y. Chang, G.R. Chen, Y.T. Xu, L.Z. Dai, Modification of epoxy resin through the self-assembly of a surfactant-like multi-element flame retardant, J. Mater. Chem. A 4 (9) (2016) 3462–3470.
[26] Z.-B. Shao, M.-X. Zhang, Y. Li, Y. Han, L. Ren, C. Deng, A novel multi-functional polymeric curing agent: synthesis, characterization, and its epoxy resin with simultaneous excellent flame retardance and transparency, Chem. Eng. J. 345 (2018) 471–482.
[27] J. Zhang, Q. Kong, D.-Y. Wang, Simultaneously improving the fire safety and mechanical properties of epoxy resin with Fe-CNTs via large-scale preparation, J. Mater. Chem. A 6 (15) (2018) 6376–6386.
[28] Z. Li, L. Liu, A. Jimenez Gonzalez, D.-Y. Wang, Bioinspired polydopamine-induced assembly of ultrafine Fe(OH)3 nanoparticles on halloysite toward highly efficient fire retardancy of epoxy resin via an action of interfacial catalysis, Polym. Chem. 8 (26) (2017) 3926–3936.
[29] J.F. Curry, T.F. Babuska, T.A. Furnish, P. Lu, D.P. Adams, A.B. Kustas, B.L. Nation, M.T. Dugger, M. Chandross, B.G. Clark, B.L. Boyce, C.A. Schuh, N. Argibay, Achieving ultralow wear with stable nanocrystalline metals, Adv. Mater. 30 (32) (2018), 1802026.
[30] S. Das, D. Lahiri, D.-Y. Lee, A. Agarwal, W. Choi, Measurements of the adhesion energy of graphene to metallic substrates, Carbon 59 (2013) 121–129.
[31] B.A. Krick, A.A. Pitenis, K.L. Harris, C.P. Junk, W.G. Sawyer, S.C. Brown, H. D. Rosenfeld, D.J. Kasprzak, R.S. Johnson, C.D. Chan, G.S. Blackman, Ultralow wear fluoropolymer composites: nanoscale functionality from microscale fillers, Tribol. Int. 95 (2016) 245–255.
[32] W.G. Sawyer, N. Argibay, D.L. Burris, B.A. Krick, Mechanistic studies in friction and wear of bulk materials, Annu. Rev. Mater. Res. 44 (1) (2014) 395–427.
[33] F. Li, K.-A. Hu, J.-L. Li, B.-Y. Zhao, The friction and wear characteristics of nanometer ZnO filled polytetrafluoroethylene, Wear 249 (10) (2001) 877–882.
[34] S.E. McElwain, T.A. Blanchet, L.S. Schadler, W.G. Sawyer, Effect of particle size on the wear resistance of alumina-filled PTFE micro- and nanocomposites, Tribol. Trans. 51 (3) (2008) 247–253.
[35] N. Yoshimichi, S. Hitoshi, Frictional force microscopic anisotropy on (001) surfaces of alkali halides and MgO, Jpn. J. Appl. Phys. 39 (7S) (2000) 4497.
[36] B.R. Burroughs, J.-H. Kim, T.A. Blanchet, Boric acid self-lubrication of B_2O_3-filled polymer composites, Tribol. Trans. 42 (3) (1999) 592–600.